2026 IEEE International Conference on Robotics and Automation (ICRA 2026)
June 1-5, 2026. Vienna, Austria

Velocity-Based Admittance-Impedance Control with Contact Compliance Modeling for Robust Dual-Arm Manipulation

Samriddhi Dubey[1*], Yash Kashiv[1*], Shreyas Kumar[2] , Siddhi Jain[3], Rajesh Kumar[3], and H. J. Palanthandalam-Madapusi[1]

***Abstract*— Many industrial and commercial manipulators provide only position and velocity control interfaces, making direct regulation of contact forces challenging. In dual-arm manipulation, this limitation prevents stable force closure and consistent control of the object wrench. We present a control framework that combines contact-level admittance and object-level impedance to compute velocity commands for both arms. The contact admittance law maps force errors into velocity corrections, while the object impedance relation regulates the net wrench on the object. Together, these laws generate joint velocities through the stacked Jacobian, ensuring consistent integration of force and motion objectives. Contact compliance is explicitly modeled using linear spring–damper elements. The analysis of closed-loop error dynamics shows how the stiffness and damping parameters of the contact compliance influence the frequency response of the error dynamics. Experiments with a dual-arm setup with two heterogeneous velocity-controlled manipulators validate the framework and the theoretical predictions. Results confirm accurate force regulation, disturbance rejection, and stable cooperative lifting under different contact padding conditions.**

The proposed approach establishes a velocity-based method for dual-arm force closure with contact compliance.

I. INTRODUCTION

Most commercial robot arms operate in position or velocity control. Torque-controlled manipulators allow precise force regulation and compliant interaction, but their use outside research and human–robot interaction is limited by cost, sensor needs, and safety certification. Consequently, contact-aware manipulation on widely available platforms remains restricted.

This limitation is especially critical in bimanual settings, where tasks like lifting, stabilizing under load, or coordinated release require regulating both internal forces for grasp stability and external wrenches for object motion. Prior works that have tackled these challenges usually assumes low-level torque access [1]–[4] and accurate actuation models. Some approaches circumvent this challenge by utilizing an admittance-based strategy with Force-Torque sensors at the end effector [5], [6]. In practice, however, implementing such force-aware velocity control on hardware introduces challenges due to sensor noise and delays as it may lead to velocity oscillations depending on the contact conditions. This is usually overcome by introducing physical passive compliance in the form of silicone or foam padding at the contacts. While some studies have examined how compliance at contact influences grasp stiffness and stability [7], largely, there is limited literature available on the analysis of how compliance at contact affects a velocity-based strategy.

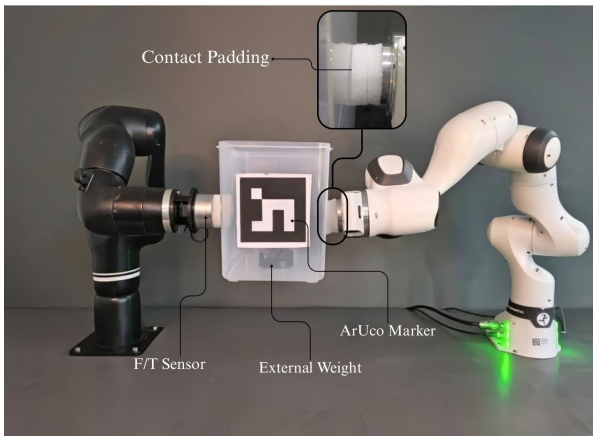

Fig. 1: Experimental setup. Addverb Heal (left) and Franka FR3 (right) collaboratively grasp an open-top box with foam pads at the robot end effectors. An external force/torque (F/T) sensor is mounted at the Heal wrist, while an Intel RealSense depth camera tracks an ArUco marker on the box to estimate object pose.

In this work, we address this gap with a velocity-based control framework that reproduces key features of torque control compliance, force-aware coordination, and disturbance rejection. At the object level, a kinematic impedance law adapts desired motion to external wrenches and maps it to end-effector velocities via grasp kinematics. At the robot level, wrench-based velocity admittance regulates each arm's response to its local contact wrench, allowing compliant yielding under perturbations. Together, these layers enable the system to withstand object-level disturbances while remaining compliant to unexpected interactions at the platform level. In addition, we model and analyze the closed-loop error dynamics to determine how compliance at contact points impact the closed loop; acting as a passive high-pass filter between the noisy wrench signal and the velocity input.

We implement the method on a dual-arm experimental setup with two heterogeneous velocity-controlled manipulators using different wrench estimation modalities. Experiments demonstrate that the system maintains secure force closure, resists object disturbances, and yields compliantly under platform perturbations. Theoretical analysis explains the observed behavior with various contact compliances and

* Equal contribution.

This work was supported by Addverb Technologies Pvt. Ltd. The authors are also grateful for inputs from Siddhi Jain, helpful discussions with Barat S and Roshan A. Chavan, and support for simulations from Kshitij Giri.

[1] Samriddhi Dubey, Yash Kashiv, and H. J. Palanthandalam-Madapusi are with the IITGN Robotics Lab, Department of Mechanical Engineering, IIT Gandhinagar, India.

guides parameter selection. The results suggest that contact-aware, collaborative manipulation typically avoided due to concerns of safety or feasibility on velocity-controlled platforms can be achieved using simple, implementable control structures and passive compliance mechanisms. Furthermore, the closed-loop error analysis in this paper informs the choice of contact parameters and feasibility of the proposed scheme in various conditions. Delays in FT sensor readings are also known to drive unstable oscillations, but an analysis of delays will be addressed in future work.

II. RELATED WORK

Torque-centric dual-arm manipulation approaches in [1]–[4] specify object-frame impedance and internal/external force regulation with joint-level authority and sensing, including adaptive or coordinated impedance controllers for cooperative manipulation.

Among admittance-based formulations, hierarchical kinematic frameworks combine cooperative-space admittance with task-priority optimization for safe dual arm execution [5]. Projected Force Admittance Control integrates grasp-space projection with admittance to modulate pose under contact [6]. These works do not focus on contact compliance modeling or analyze the impact of sensor noise in the closed loop. Contact compliance has been analyzed in terms of its influence on grasp stability and stiffness [7], but such studies primarily address static grasp analysis rather than velocity-based manipulation under noisy wrench feedback.

Model-predictive transport and handling approaches use observers and disturbance estimation to maintain object trajectories under external wrenches, often regulating interaction via admittance or inner velocity loops [8]. Dynamic dual-arm skills address fast grabbing, coordinated throwing, and high-momentum exchange, emphasizing task-level performance and grasp transitions [9]. These works demonstrate the potential of coordinated actions but do not focus on velocity-only compliance.

In contrast, our framework operates entirely through velocity commands, composing an object-level kinematic impedance behavior with local wrench-to-velocity admittance. By explicitly modeling contact compliance (padding) and analyzing its stabilizing effect under noisy wrench feedback, we enable compliant dual-arm manipulation on platforms without torque interfaces.

III. MATHEMATICAL FRAMEWORK

With the goal to regulate contact forces while ensuring compliant cooperative motion of the object, the architecture proposed in Fig. 2, proceeds in four stages. First, sensing and estimation provide the object state, measured forces, and external disturbances. At the contact level, the controller distributes and corrects forces through an admittance law to maintain feasible contact. At the object level, motion is shaped by an impedance relation that provides compliant responses to external loads. Finally, a joint–space synthesis stage combines the contact and object-level commands into coordinated joint velocity inputs for both manipulators.

A. Force Closure with Velocity Control

Consider a rigid object being cooperatively manipulated by m robotic arms, where each arm interacts with the object through a designated contact point. At each contact $i \in \{1, 2, \dots, m\}$, the applied wrench is $F_i = \begin{bmatrix} f_i^\top & \tau_i^\top \end{bmatrix}^\top \in \mathbb{R}^6$, where $f_i \in \mathbb{R}^3$ is the contact force and $\tau_i \in \mathbb{R}^3$ is the contact torque. Stacking across all contacts yields

$$F = \begin{bmatrix} F_1^\top & F_2^\top & \cdots & F_m^\top \end{bmatrix}^\top \in \mathbb{R}^{6m}.$$

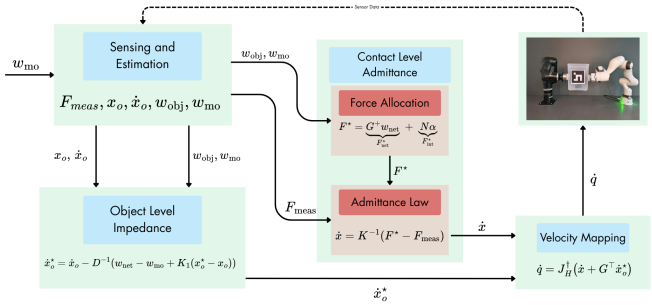

Fig. 2: Control architecture for dual-arm manipulation. The framework combines contact-level admittance with object-level impedance, and maps the resulting commands into joint velocities for two heterogeneous velocity-controlled manipulators.

In the following, we focus on regulating the force component f_i at each contact and drop torques at contact for simplicity. Thus, for the subsequent development we take $F_i \in \mathbb{R}^3$ and $F \in \mathbb{R}^{3m}$, while the framework is easily extendable to full wrenches.

Let $F^\star \in \mathbb{R}^{3m}$ denote the desired stacked contact force vector. In the context of grasping, we define *force closure* as the condition under which the set of contact forces can balance any external wrench acting on the object, subject to friction constraints. To enforce this, $F^\star$ is constructed to counteract the external wrench on the object.

Desired Wrench Construction: The desired contact force distribution can be understood as the sum of three components [10]. The *equilibrating term* counteracts external disturbances and maintains the object in static equilibrium. The *motive term* corresponds to the wrench required to generate or sustain motion, ensuring the object follows a commanded trajectory. The *internal term* lies in the null space of the grasp matrix and therefore does not affect the net object wrench; instead, it is adjusted to impose preload and satisfy frictional feasibility conditions. Together, we have

$$F^\star = \underbrace{G^+ w_{\text{eq}}}_{F_{\text{eq}}^\star} + \underbrace{G^+ w_{\text{mo}}}_{F_{\text{mo}}^\star} + \underbrace{N\alpha}_{F_{\text{int}}^\star}, \tag{1}$$

Here $G \in \mathbb{R}^{6\times 3m}$ is the grasp matrix mapping stacked contact forces to the net object wrench, and $N \in \mathbb{R}^{3m\times k}$ is a matrix whose columns span the null space of G ($GN = 0$), representing directions of internal forces that do not affect the net object wrench. $\alpha \in \mathbb{R}^k$ specify an arbitrary k-dimensional vector with $k = \dim(\text{Null}(G))$. We

define the net contact force as the sum of the equilibrating and motive components $F^{\star}_{\text{net}} = G^{+}\left(w_{\text{eq}} + w_{\text{mo}}\right)$ and with defining $w_{\text{net}} = w_{\text{eq}} + w_{\text{mo}}$, we obtain

$$F^{\star} = \underbrace{G^{+} w_{\text{net}}}_{F^{\star}_{\text{net}}} + \underbrace{N\alpha}_{F^{\star}_{\text{int}}}. \tag{2}$$

The net wrench w_{net} is obtained from measured contact forces $F_{\text{net}} \in \mathbb{R}^{3m}$ as

$$\begin{aligned} F^{\star}_{\text{net}} &= G^{+} w_{\text{net}}, & w_{\text{net}} &= w_{\text{mo}} - \hat{w}_{\text{ext}}, \\ \hat{w}_{\text{ext}} &= \hat{w}_{\text{obj}} - w_{\text{mo}}, & \hat{w}_{\text{obj}} &= G F_{\text{meas}}. \end{aligned} \tag{3}$$

where $w_{\text{mo}} \in \mathbb{R}^{6}$ denotes the commanded object wrench associated with the motive part, $\hat{w}_{\text{obj}}$ is the measured object wrench, and $\hat{w}_{\text{ext}}$ is the estimated external disturbance. In the case in which only static equilibrium and disturbance rejection of the object is desired (no commanded motion); we set $w_{\text{mo}} = 0$ and consequently $F^{\star}_{\text{mo}} = 0$, and the net wrench reduces to

$$w_{\text{net}} = -\hat{w}_{\text{obj}}, \qquad F^{\star}_{\text{net}} = -G^{+}\hat{w}_{\text{obj}}, \tag{4}$$

so that the commanded forces simply cancel the measured object wrench. On the other hand, when a specific motion such as throwing is commanded, the controller enforces the motive wrench. The resulting net wrench using (3) becomes

$$w_{\text{net}} = 2w_{\text{mo}} - \hat{w}_{\text{obj}}, \tag{5}$$

which combines disturbance rejection with the motion command. In this way, the formulation unifies equilibrium control and motion generation within the same framework.

In addition to the net force component $F^{\star}_{\text{net}}$, the desired contact force distribution also contains an internal component. These forces lie in the null space of the grasp matrix and therefore do not contribute to the net object wrench:

$$F^{\star}_{\text{int}} = N\alpha, \qquad GN = 0, \tag{6}$$

While they do not affect the object's wrench, internal forces are used to regulate preload and satisfy frictional feasibility at the contacts.

To ensure feasibility, α is chosen so that the contact forces satisfy Coulomb friction constraints. Decomposing the contact force at contact point i into its normal and tangential components $(f_{n,i}, f_{t1,i}, f_{t2,i})$, the admissible region is

$$\sqrt{f_{t1,i}^{2} + f_{t2,i}^{2}} \le \mu_i f_{n,i}, \qquad i = 1, 2, \tag{7}$$

where μ_i is the friction coefficient at contact i. In practice, the quantities $f_{n,i}, f_{t1,i}, f_{t2,i}$ are obtained directly from the force/torque sensors mounted at each end-effector

For the case of two contacts, the internal force subspace is one–dimensional and corresponds to equal and opposite forces along the line connecting the two contact points. Let $r_1, r_2 \in \mathbb{R}^3$ denote the contact position vectors expressed in the object frame, and let n_i be the unit surface normal at contact i. The internal force direction is then given by

$$\hat{u} = \frac{r_2 - r_1}{\|r_2 - r_1\|}. \tag{8}$$

The minimal admissible preload coefficient is computed as

$$\alpha_{\min} = \max_{i=1,2} \frac{\max\left(0,\ \sqrt{f_{t1,i}^{2} + f_{t2,i}^{2}}/\mu_i - f_{n,i}\right)}{\hat{u} \cdot n_i}, \tag{9}$$

and the applied value is chosen as

$$\alpha \leftarrow \alpha_{\min} + \epsilon, \qquad \epsilon > 0, \tag{10}$$

which ensures a safety margin above the minimum required preload. The resulting internal forces at the two contacts are

$$F^{\star}_{\text{int},1} = +\alpha\hat{u}, \qquad F^{\star}_{\text{int},2} = -\alpha\hat{u}. \tag{11}$$

For multi–contact grasps ($m \ge 3$), the internal force subspace has dimension $3m - 6$. In this case, the vectors α are computed by solving a quadratic program that enforces friction and unilateral contact constraints while minimizing the deviation from the nominal distribution $F^{\star}$, thereby achieving force closure as described in [10].

B. Admittance and Object-Level Impedance Control with Velocity Control

Having defined the desired contact wrench $F^{\star}$ and the measured contact forces F_{meas} from the FT sensors, we now embed these quantities in a velocity–based control framework.

At the contact level, an admittance law regulates the wrench error $e_m = F^{\star} - F_{\text{meas}}$ through the velocity command

$$\dot{x} = K^{-1}(F^{\star} - F_{\text{meas}}), \tag{12}$$

where $K \in \mathbb{R}^{6\times 6}$ is a positive–definite admittance gain matrix. This law maps deviations in measured contact force into corrective velocity inputs, so that the commanded motion reduces the force error at each contact.

At the object level, the dual–arm system regulates the net wrench applied to the object. pose is denoted by $x_o \in SE(3)$, with velocity $\dot{x}_o \in \mathbb{R}^{6}$. The object–level impedance law specifies the commanded velocity as

$$\dot{x}_o^{\star} = \dot{x}_o - D^{-1}(w_{\text{net}} - w_{\text{mo}} + K_1(x_o^{\star} - x_o)), \tag{13}$$

where $K_1, D \in \mathbb{R}^{6\times 6}$ are desired stiffness and damping matrices. This relation ensures that discrepancies between the commanded and desired wrench, as well as between the desired and actual pose, are corrected through compliant velocity adjustments.

Together, the contact–level admittance (12) and the object–level impedance (13) yield consistent velocity commands. The former enforces the distribution of forces at individual contacts, while the latter regulates the net object behavior, enabling compliant and coordinated dual–arm manipulation.

C. Commanded Robot Velocities

The contact–level admittance produces $\dot{x} \in \mathbb{R}^{3m}$, while the object–level impedance generates the desired object twist $\dot{x}_o^{\star} \in \mathbb{R}^{6}$. Therefore, $G^{\top}\dot{x}_o^{\star} \in \mathbb{R}^{3m}$ represents the corresponding contact velocities under the no–slip assumption. The stacked hand Jacobian is $J_H \in \mathbb{R}^{3m\times n_q}$, where n_q is

Algorithm 1 Dual-Arm Velocity Control for Grasp Regulation and Object-Level Motion

Require: $x_o, \dot{x}_o, x_o^\star, F_{\text{meas}}, w_{\text{mo}}$; gains K, K_1, D; models G, N, J_H
Ensure: $\dot{q}$

$\hat{w}_{\text{obj}} \leftarrow G\, F_{\text{meas}}$
$\hat{w}_{\text{ext}} \leftarrow \hat{w}_{\text{obj}} - w_{\text{mo}}$
$w_{\text{net}} \leftarrow w_{\text{mo}} - \hat{w}_{\text{ext}}$ ▷ $= 2w_{\text{mo}} - \hat{w}_{\text{obj}}$; if $w_{\text{mo}} = 0$, $w_{\text{net}} = -\hat{w}_{\text{obj}}$
choose α to satisfy friction/unilateral constraints (two-contact closed form or QP for $m \geq 3$)
$F^\star \leftarrow G^+ w_{\text{net}} + N\,\alpha$
$\dot{x} \leftarrow K^{-1}\big(F^\star - F_{\text{meas}}\big)$
$\dot{x}_o^\star \leftarrow \dot{x}_o - D^{-1}\big(w_{\text{net}} - w_{\text{mo}} + K_1(x_o^\star - x_o)\big)$
$\dot{q} \leftarrow J_H^\dagger\big(\dot{x} + G^\top \dot{x}_o^\star\big)$

the total number of robot joints across both manipulators. The joint velocity command is then given by

$$\dot{q} = J_H^\dagger\left(\dot{x} + G^\top \dot{x}_o^\star\right), \qquad \dot{q} \in \mathbb{R}^{n_q}. \tag{14}$$

The resulting vector $\dot{q}$ is naturally partitioned into the joint velocity commands of each arm according to their degrees of freedom. The entire framework is summarized in Algorithm 1.

D. Effect of Contact Compliance on Two-Arm Force Closure

In dual-arm manipulation with force closure, contact compliance and sensor noise can destabilize the system. Noise in the measured forces enters the admittance law, where even small perturbations may be amplified into alternating velocity commands. These rapid sign changes manifest as high-frequency oscillations at the end-effectors, which may transiently reduce normal contact forces and risk loss of contact. This effect is seen in experiments leading to frequent loss of contact and drops of the held object as highlighted in later sections. To analyze this effect and provide a basis for understanding how compliance parameters influence the oscillations, we model the measured forces at m contacts as

$$F_{\text{meas}} = F + n, \tag{15}$$

where $F \in \mathbb{R}^{3m}$ are the true contact forces and n is zero-mean Gaussian sensor noise. Using the desired wrench formulation in Eq. (2), the net wrench expression in Eq. (5), and the projection matrix $P = G^+G$, the commanded force distribution becomes

$$F^\star = 2G^+ w_{\text{mo}} - PF - Pn + N\alpha. \tag{16}$$

The measured error is defined as

$$e_{\text{m}} = F^\star - F_{\text{meas}}, \tag{17}$$

which can be decomposed into net and internal components using the projection matrix $P = G^+G$ as

$$e_{\text{net}} = Pe_{\text{m}}, \qquad e_{\text{int}} = (I - P)e_{\text{m}}, \tag{18}$$

so that $e_{\text{m}} = e_{\text{net}} + e_{\text{int}}$.

Closed-Loop Contact Dynamics.: Assuming isotropic gains and the same isotropic contact compliance across all contacts, the stiffness, damping, and gain matrices are

$$K_s = k_s I, \qquad D_s = d_s I, \qquad K = kI, \tag{19}$$

with $k_s, d_s, k \in \mathbb{R}_+$ scalars and I being the 6×6 identity matrix. The contact pad is modeled as a linear isotropic spring–damper system, leading to the force relations

$$F = K_s x + D_s \dot{x}, \tag{20a}$$
$$\dot{F} = K_s \dot{x} + D_s \ddot{x}. \tag{20b}$$

In the admittance law of Eq. (12), substituting F_{meas} from Eq. (15), differentiating the velocity term, and using the contact pad dynamics in Eq. (20b), we obtain

$$\dot{F} = K_s A(F^\star - F - n) + D_s A(\dot{F}^\star - \dot{n}), \tag{21}$$

where $A = (K + D_s)^{-1}$. This expression explicitly shows the effect of compliance and noise on the force evolution.

Error and Projected Error Dynamics: Define the true error as

$$e = F^\star - F, \qquad \dot{e} = \dot{F}^\star - \dot{F}, \tag{22}$$

therefore

$$e_m = F^\star - F_{\text{meas}} = e - n. \tag{23}$$

Substituting the force dynamics from Eq. (21) into $\dot{e}$ and introducing the shorthand

$$T^{-1} = K_s A, \qquad B = KA = (I - D_s A),$$

yields the error dynamics

$$\dot{e} + T^{-1}e = B\,\dot{F}^\star + T^{-1}n + D_s A\,\dot{n}. \tag{24}$$

Since $e_m = e - n$, differentiation gives $\dot{e}_m = \dot{e} - \dot{n}$, and substitution into (24) yields the measured error dynamics

$$\dot{e}_m + T^{-1}e_m = B\,\dot{F}^\star - B\,\dot{n}. \tag{25}$$

Using the decomposition in Eq. (18), the measured error splits into net and internal components

$$\dot{e}_{\text{net}} + T^{-1}e_{\text{net}} = B\,P\,\dot{F}^\star - B\,P\,\dot{n}, \tag{26}$$
$$\dot{e}_{\text{int}} + T^{-1}e_{\text{int}} = B\,(I - P)\dot{F}^\star - B\,(I - P)\dot{n}. \tag{27}$$

Equations (25)–(27) show that both the measured error and its projected components evolve as first–order linear systems.

Resulting Force Dynamics: From Eq. (16), subtracting $(F + n)$ from both sides yields

$$F^\star - F - n = 2G^+ w_{\text{mo}} + N\alpha - (I + P)(F + n). \tag{28}$$

Differentiating Eq. (28) gives

$$\dot{F}^\star - \dot{n} = 2G^+ \dot{w}_{\text{mo}} - P\dot{F} + N\dot{\alpha} - (P\dot{n} + \dot{n}). \tag{29}$$

Substituting (28) and (29) into Eq. (21), and collecting all $\dot{F}$ terms on the left-hand side, the closed-loop force evolution is obtained as

$$\begin{aligned}(I + \gamma P)\dot{F} \;=\; & -\tau^{-1}(I + P)(F + n) \\ & + \tau^{-1}(2G^+ w_{\text{mo}} + N\alpha) \\ & + \gamma(2G^+ \dot{w}_{\text{mo}} + N\dot{\alpha}) - \gamma(P\dot{n} + \dot{n}).\end{aligned} \tag{30}$$

Using the isotropic gains of Eq. (19), the scalar quantities are defined as

$$\begin{aligned} A &= (k+d_s)^{-1} I, \qquad \tau = \tfrac{k+d_s}{k_s}, \\ \gamma &= \tfrac{d_s}{k+d_s}, \qquad T^{-1} = K_s A = \tfrac{1}{\tau} I. \end{aligned} \tag{31}$$

For high-frequency analysis, the slowly varying feedforward terms ($2G^{+}w_{\text{des}}$, $N\alpha$) and explicit noise-derivative terms can be neglected. The resulting approximation is

$$\begin{aligned} (I+\gamma P)\dot{F} \;\approx\; & -\tau^{-1}(I+P)(F+n) \\ & +\gamma\,(2G^{+}\dot{w}_{\text{mo}} + N\dot{\alpha}). \end{aligned} \tag{32}$$

This form explicitly shows how isotropic stiffness and damping gains shape the closed-loop evolution of the contact forces.

Net and Internal Error Dynamics: Combining the projected error relations (26)–(27) with the commanded force distribution (16) gives

$$\begin{aligned} \dot{e}_{\text{net}} + T^{-1} e_{\text{net}} &= B\Big(2G^{+}\dot{w}_{\text{mo}} - P\dot{F} - P\dot{n}\Big) - B\,P\dot{n}, \\ \dot{e}_{\text{int}} + T^{-1} e_{\text{int}} &= B\,N\dot{\alpha} - B\,(I-P)\dot{n}, \end{aligned} \tag{33}$$

with $B = KA = \frac{K}{K+d_s} I = \beta I$.

The internal error dynamics depend only on $N\dot{\alpha}$ and $(I-P)\dot{n}$. The net error dynamics still include $P\dot{F}$, which is resolved by projecting (32). Using $P^2 = P$, $PN = 0$, and $P(I+P) = 2P$, and defining $Q := I + \frac{1}{1+\gamma} P$ for convenience, we obtain from (33)

$$\dot{e}_{\text{net}} + QT^{-1} e_{\text{net}} = \tfrac{K}{K+d_s}(2G^{+}\dot{w}_{\text{mo}}) - Q\dot{n}, \tag{34}$$

$$\dot{e}_{\text{int}} + T^{-1} e_{\text{int}} = \tfrac{K}{K+d_s}\, N\dot{\alpha} - (I-P)\dot{n}. \tag{35}$$

Thus both the net and internal components behave as first-order filters. The corner frequencies are $a_{\text{net}} = \frac{2+\gamma}{1+\gamma}\,\frac{1}{\tau}$ for the net error component and $a_{\text{int}} = \frac{1}{\tau}$ for the internal component. Reducing stiffness k_s increases τ and therefore lowers both corner frequencies, attenuating high-frequency oscillations. Increasing damping d_s increases γ (and reduces β), which lowers the net error corner frequency and reduces noise transmission in that channel. These predictions will be verified experimentally.

IV. Experimental Setup

Experiments were conducted with two heterogeneous manipulators sharing a workspace: a 6-DoF Addverb Heal and a 7-DoF Franka Emika FR3, both commanded through velocity interfaces in ROS. Heal was equipped with an external six-axis force/torque (F/T) sensor at the wrist, while the Franka relied on its integrated joint torque sensors.

The manipulated object was a rigid open-top box with outer dimensions $22\times16\times24$ cm (length $\times$ breadth $\times$ depth) and mass 0.36 kg. During disturbance trials, additional payloads of 0.25, 0.5, and 0.75 kg (unknown to the controller) were sequentially placed inside the box. Each robot grasped an opposing vertical face at mid-height using flat custom end-effectors. To vary compliance, three contact conditions were tested: rigid (no padding), a single foam layer of 1.5 cm per arm, and a double foam stack totaling 3 cm per arm.

At the grasp contacts, the Heal's x-axis and the Franka's y-axis were aligned with the face normals and pointed outward from the box. As a result, pressing forces appeared negative (e.g., a 7 N preload logged as $F_{\text{des}} = -7$ N), ensuring consistent sign conventions. The box pose was tracked via an ArUco marker and RealSense depth camera, with estimates supplied to the velocity-level controller. The complete setup is shown in Fig. 1.

V. Experiments and Evaluation

This section reports four sets of experiments: (i) contact compliance validation, (ii) force closure under external payloads, (iii) cooperative lifting with weight compensation, and (iv) restoration under large perturbations. The proposed object–level impedance and force–closure framework was evaluated through hardware and simulation studies. The experiments were designed to first validate contact compliance on the Heal using no, single, and double padding, and in MuJoCo simulations with rigid contact and compliant end-effector springs of stiffness 500 N/m and 50 N/m, with Gaussian noise added force/torque measurements.

A. Validation of Contact Padding

To assess the role of contact compliance, cooperative lifting experiments were performed under three conditions: no padding, single padding, and double padding. Across ten repeated trials for each condition, the outcomes summarized in Table II show that no–padding runs consistently failed, single padding succeeded in 40% of cases, and double padding achieved a 100% success rate. These observations highlight the necessity of analyzing how contact compliance influences force regulation and grasp stability.

TABLE II: Success rates of cooperative lifting trials under different contact conditions. Success is defined as both manipulators maintaining a stable grasp without slip or loss of contact for the full trial duration.

Condition	No Padding	Single Padding	Double Padding
Success (runs)	0/10	4/10	10/10
Success Rate	0%	40%	100%

1) Unimanual (Heal): The admittance controller was tested on the Heal with the object fixed on a table. A preload of $F_{\text{des}} = 7$ N was commanded along the surface normal, such that the arm pressed against the box while the table provided the reaction force. According to the admittance law (12), the commanded velocity $\dot{x} = K^{-1}(F^{\star} - F_{\text{meas}})$ regulates the measured force toward $F^{\star}$.

Figure 3(a–c) shows that without padding, noise led to oscillatory responses, while single and double foam layers progressively improved performance. Table I quantifies this effect: the mean force shifted from -9.17 N (no pad) toward the target -7 N with single (-6.99 N) and double padding (-6.88 N); the standard deviation reduced from 9.73 N to 2.33 N and 1.26 N, and RMSE from 18.87 N to 13.94 N.

The frequency spectra in Fig. 3(d) confirm the same trend, with the $\sim$4 Hz mode dominant in the no–padding case and strongly attenuated under increased compliance.

TABLE I: Force tracking statistics (Mean, Standard Deviation, RMSE) across unimanual (Heal hardware), Heal MuJoCo simulations, and dual-arm (Heal + Franka) cases. The desired force was $F_{\text{des}} = -7$ N for hardware and dual trials, and $+7$ N for simulation. In MuJoCo, three cases were tested: rigid contact (No Pad) and compliant end-effector springs with stiffness values of 500 N/m and 50 N/m. Across all trials, lower stiffness compliance yielded mean forces closer to the desired value, with standard deviation and RMSE consistently decreasing as compliance increased, thereby confirming that added compliance improves stability.

	Unimanual Exp. (Heal hardware)			**Unimanual Heal (MuJoCo)**			**Dual-Arm (Heal + Franka)**					
	No Pad	Single	Double	No Pad	Compliance		Heal			Franka		
					500 N/m	50 N/m	No Pad	Single	Double	No Pad	Single	Double
Mean [N]	-9.172	-6.996	-6.882	5.945	5.767	6.178	-6.953	-6.568	-6.917	-7.632	-7.496	-6.941
Std Dev [N]	9.727	2.328	1.263	2.846	2.569	2.061	4.257	2.520	0.823	5.316	2.896	0.663
RMSE [N]	18.868	14.188	13.939	3.035	2.849	2.219	14.588	13.800	13.941	15.568	14.783	13.957

These results show that padding reduces bias, variance, and oscillations as predicted by the framework.

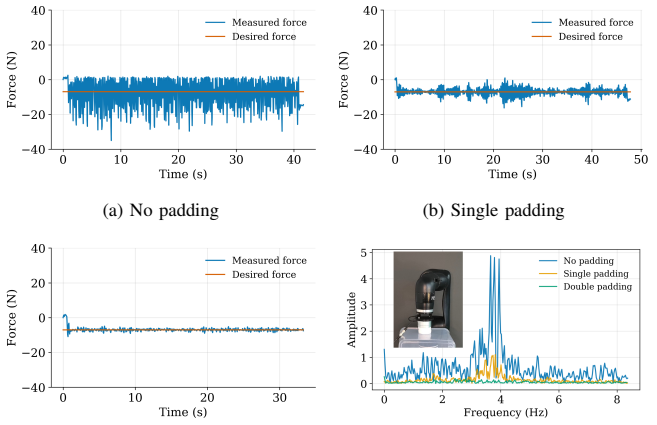

(a) No padding (b) Single padding

(c) Double padding (d) FFT of force error (all three conditions)

Fig. 3: Heal results at $|F_{\text{des}}| = 7$ N. (a–c) Force–time responses for no, single, and double padding. (d) FFT of the force error showing attenuation of the ~ 4 Hz component and reduced broadband energy with increased padding.

2) Dual arm (Heal + Franka): Building on the unimanual results, we next evaluated cooperative regulation with both Heal and Franka applying $F_{\text{des}} = 7$ N. The box was placed between the two manipulators, and each arm applied force on opposite faces along the contact normal. Figure 4 shows the force responses under three contact conditions. Without padding, both arms exhibited large oscillations; single padding reduced fluctuations, while double padding yielded tightly bounded forces around the reference.

Table I quantifies these improvements: for Heal, the standard deviation decreased from 4.26 N (no pad) to 0.82 N (double), while for Franka it reduced from 5.32 N to 0.66 N, with RMSE values showing a similar trend. The FFT spectra in Fig. 4(g–h) confirm that 3–5 Hz oscillations present without padding are attenuated as compliance increases.

3) MuJoCo Simulation Validation: We reproduced the task in MuJoCo at a desired force of $F_{\text{des}} = 7$ N with the box placed on the ground. The Heal end-effector was modeled with a compliant pad represented as a linear spring in the surface-normal direction. The stiffness of this virtual spring was tunable, allowing us to test three cases: hard contact, high stiffness ($k = 500$ N/m), and low stiffness ($k = 50$ N/m). Gaussian noise was injected into the force channel to reproduce the noise observed in hardware.

As seen in Table I, hard contact leads to persistent oscillations with a standard deviation exceeding 2.8 N. Increasing

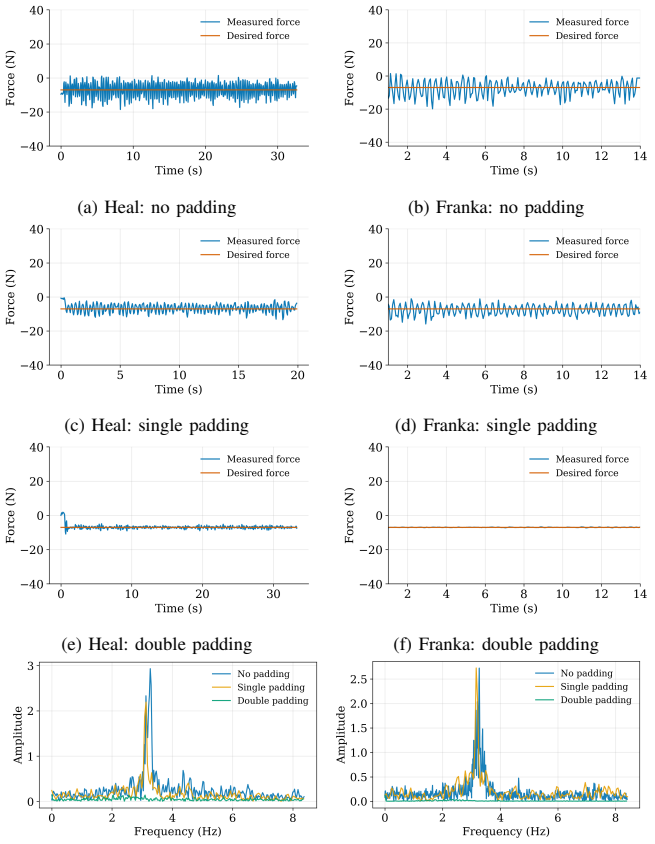

(a) Heal: no padding (b) Franka: no padding

(c) Heal: single padding (d) Franka: single padding

(e) Heal: double padding (f) Franka: double padding

(g) FFT comparison for Heal forces (h) FFT comparison for Franka forces

Fig. 4: Dual arm force regulation at $F_{\text{des}} = 7$ N. Time–domain responses for Heal (left) and Franka (right) under three padding conditions, with FFT comparison for Heal (bottom).

stiffness to $k = 500$ N/m reduces but does not fully eliminate these fluctuations. The low-stiffness case ($k = 50$ N/m) achieves the most stable and accurate tracking. Overall, the simulations confirm the same behavior observed in the unimanual Heal and dual arm hardware experiments.

4) Error Dynamics Corner Frequencies: To correlate the experimental results with the predicted error dynamics in (35) and (34), we estimate the stiffness of the single pad to be $20,430 N/m$ and the double pad to be $9010 N/m$ using simple force-deformation tests in the lab. With these stiffnesses, with an admittance gain of $K = 0.01$, and an assumed damping of 400 Ns/m and 250Ns/m (approximately calculated to be in the overdamped region), the corner frequencies of the error dynamics (35) is calculated as $\frac{1}{\tau} = 51.075$ rad/s = 8.13 Hz for the single pad and $\frac{1}{\tau} = 36.04$

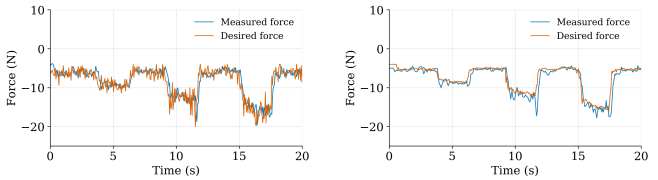

(a) Heal: force vs. time

(b) Franka: force vs. time

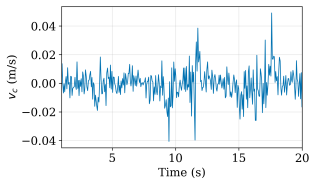

(c) Heal: contact point velocity vs. time

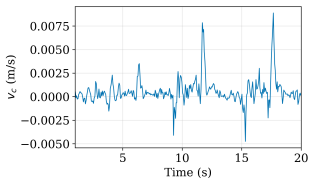

(d) Franka: contact point velocity vs. time

Fig. 5: Force closure under *external weight compensation*. Heal and Franka collaboratively held the open-top box while sequential payloads of 250 g, 500 g, and 750 g (unknown to the controller) were added. (a, b) Measured forces rise proportionally with the added weights, closely tracking the desired references above the nominal preload $F_{\text{des}} = 4$ N. (c, d) Corresponding contact point velocity responses v_c along the contact axes remain bounded and converge back to zero, demonstrating stable compensation of external disturbances.

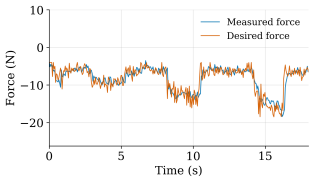

(a) Heal: force vs. time

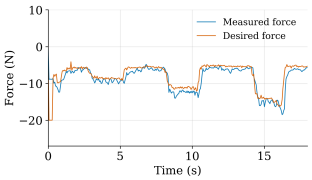

(b) Franka: force vs. time

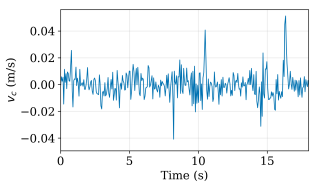

(c) Heal: contact point velocity vs. time

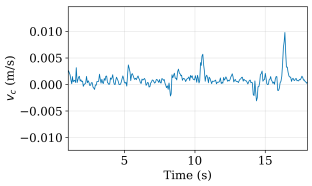

(d) Franka: contact point velocity vs. time

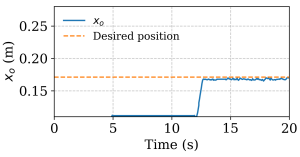

(e) Object position vs. time

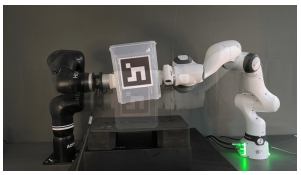

(f) Dual arm lifting experiment

Fig. 6: Object lifting with *external weight compensation*. (a, b) Heal and Franka increase normal forces above the preload to counter payloads of 250, 500, and 750 g. (c, d) Contact point velocities show bounded transients that decay to equilibrium. (e) Object trajectory during the lift. (f) Snapshot of the dual-arm experiment.

rad/s = 5.74 Hz. Although these are arrived upon using a crude estimate of damping, the addition of the contact compliances, particularly in the case of double foam pads, moves the corner frequency of the error dynamics close to the $3-5$ Hz frequency range seen in the force error. These results demonstrate a reasonably close match between theoretical predictions and experimental observations.

B. Force Closure with External Disturbances

To validate the formulation derived in Section III.A, we conducted experiments in which Heal and Franka jointly held the open-top box under incrementally applied external payloads. Payloads of 250 g, 500 g, and 750 g (unknown to the controller) were sequentially placed inside the box, thereby introducing external downward forces in addition to the nominal preload of $\epsilon = 4$ N. Figure 5 summarizes the resulting force and velocity responses.

As expected, the desired forces rose above the preload in proportion to the added payloads. Both robots tracked these references: measured forces increased from about -7 N to -20 N, consistent with predicted setpoints, with a safety limit of -20 N. The F/T sensors detected the added load, and the admittance controller adjusted velocities to generate compensating forces. Corresponding Cartesian velocity responses showed bounded transients that quickly decayed to zero once equilibrium was restored.

These results demonstrate that the proposed velocity-based control successfully compensates for external disturbances by sensing the increased load through the F/T sensors and regulating the contact forces until equilibrium is restored.

C. Object Lifting with External Force Compensation

To validate the object-level impedance law in (13), we repeated the 17 cm lifting task while embedding explicit compensation for external loads. During the lift, additional payloads of 250 g, 500 g, and 750 g were sequentially placed inside the open-top box, introducing downward disturbances on top of the nominal preload of $\epsilon = 4$ N. Figure 6 summarizes the results. Subfigures (a)–(b) show the force regulation for Heal and Franka: in both cases, measured forces increased from approximately -7 N at preload to nearly -20 N under the heaviest load, closely tracking the desired references predicted by $F^\star$. Subfigures (c)–(d) report the corresponding Cartesian velocities v_c along the contact axes: bounded transients appear immediately after each payload is added, but quickly decay as the controller converges to the new equilibrium. Subfigure (e) shows the object position trajectory, where the box is lifted smoothly to the commanded height of 17 cm without slip, despite the added disturbances. These results quantitatively validate the formulation in (13).

D. Object Impedance Behavior under Large Disturbances

Finally, we evaluated performance under perturbations during lifting. External forces were applied four times, causing temporary deviations from the commanded trajectory. In each case, the object-level impedance law in (13) restored the box to its 17 cm target, regulating both equilibrating and internal forces for compliant yet stable recovery.

Figure 7 summarizes the results. Subfigures (a)–(b) show that Heal and Franka increased contact forces adaptively while avoiding oscillations. Subfigures (c)–(d) report bounded, spring-like velocity transients that decayed rapidly. Subfigure (e) illustrates the object trajectory: although displaced by several centimeters, the box returned to the commanded height with minimal steady-state error.

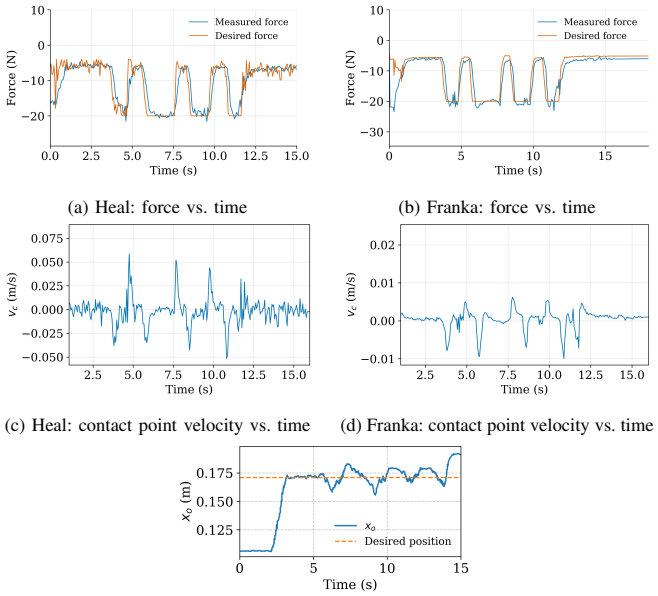

(a) Heal: force vs. time

(b) Franka: force vs. time

(c) Heal: contact point velocity vs. time

(d) Franka: contact point velocity vs. time

(e) Object position vs. time

Fig. 7: Object lifting experiment demonstrating *impedance–based restoration*. (a, b) Heal and Franka regulate normal forces, rising adaptively in response to perturbations. (c, d) Corresponding contact point velocity responses.

VI. Discussion and Conclusions

The experimental and simulation results consistently highlight the role of compliance and disturbance compensation in enabling stable force closure and cooperative manipulation.

In the unimanual Heal experiments, contact padding was found to be necessary for stability. The standard deviation of measured force decreased from nearly 10 N in the rigid case to 1.3 N with double padding, while RMSE dropped from 18.9 N to 7.5 N (Table I). Frequency-domain analysis confirmed this effect, with compliance shifting spectral energy away from destabilizing high-frequency modes.

The bimanual tests extended these observations, showing that Heal and Franka could coordinate to regulate normal forces during cooperative grasping. The MuJoCo simulations reinforced these findings under controlled conditions. By modeling the Heal pad as a tunable spring and injecting Gaussian noise to emulate sensor imperfections, the same trends were observed: hard contact led to persistent oscillations (> 4 N standard deviation), high stiffness partially mitigated them, and low stiffness ($k = 50$ N/m) achieved the most stable tracking (< 2 N variability). This agreement indicates that the observed behaviors are not hardware-specific but arise from the underlying control structure. In the first stage, we examined *force closure with external weight compensation*, where sequential payloads of 250 g, 500 g, and 750 g (unknown to the controller) were added to the open-top box. Both manipulators sensed the increased load via their F/T sensors and adaptively increased normal forces, tracking the references predicted by $F_{\text{eq}}^{\star} = G^{+} w_{\text{net}}$. This demonstrated that static equilibrium could be preserved under external loading.

Building on this, we next repeated the 17 cm *object lifting task with external weight compensation*. Here, the desired object wrench was explicitly augmented with disturbance estimates in the admittance law. As the payload increased, both manipulators raised their normal forces in proportion to the load, while Cartesian velocity responses remained bounded and decayed to zero as equilibrium was restored. The box was lifted smoothly to the commanded height of 17 cm without slip, validating the disturbance-augmented object-level control.

Finally, we subjected the system to *large perturbations* to probe its impedance behavior. External forces were applied four times and each case caused significant transient displacement, but the object-level impedance law regulated both equilibrating and restorative terms to restore the trajectory. The box consistently returned to the commanded position with negligible steady-state error, confirming stable and compliant behavior even under severe disturbances.

Taken together, these results quantitatively validate the proposed two-tier framework: contact-level admittance, augmented by compliance, with the object-level impedance law governing equilibrating and restorative responses of the object. The combination yields robust performance across static force closure, cooperative lifting under external loads, and large disturbance rejection.

The error dynamics predictions due to contact compliance and noise also matched well with experimentally observed values. The analysis in this paper informs the choice of contact parameters and feasibility of velocity-based admittance-impedance scheme under various conditions. Effect of delays in FT sensor readings will be taken up in future work.

References

[1] C. Jiao, L. Yu, X. Su, Y. Wen, and X. Dai, "Adaptive hybrid impedance control for dual-arm cooperative manipulation with object uncertainties," *Automatica*, vol. 140, p. 110232, 2022.

[2] Y. Zhang, "Adaptive coordinated impedance control for dual-arm robot symmetric bimanual tasks," *Robotics and Autonomous Systems*, vol. 193, p. 105110, 2025.

[3] X. Jing, L. Roveda, J. Li, Y. Wang, and H. Gao, "An adaptive impedance control for dual-arm manipulators incorporated with the virtual decomposition control," *Journal of Vibration and Control*, vol. 30, no. 11-12, pp. 2647–2660, 2024.

[4] H. Hu, S. Wen, and J. Yu, "Prescribed time control of position and force tracking for dual-arm robots with output error constraints," *Scientific Reports*, vol. 15, p. 3170, 2025.

[5] S. Tarbouriech, B. Navarro, P. Fraisse, A. Crosnier, A. Cherubini, and D. Sallé, "An admittance based hierarchical control framework for dual-arm cobots," *Mechatronics*, vol. 86, p. 102814, 2022.

[6] J. Gao, Y. Zhou, and T. Asfour, "Projected force–admittance control for compliant bimanual tasks," in *Proc. IEEE-RAS Int. Conf. Humanoid Robots (Humanoids)*, pp. 1–9, 2018.

[7] A. Shapiro, M. Ciocarlie, and P. K. Allen, "On the mechanics of natural compliance in frictional contacts and its effect on grasp stiffness," *IEEE Transactions on Robotics*, vol. 29, no. 3, pp. 593–602, 2013.

[8] M. Lei, M. Selvaggio, T. Wang, F. Ruggiero, C. Zhou, C. Yao, and Y. Zheng, "Dual-arm object transportation via model predictive control and external disturbance estimation," in *Proc. IEEE Int. Conf. Automation Science and Engineering (CASE)*, pp. 2328–2334, 2022.

[9] M. Bombile and A. Billard, "Dual-arm control for coordinated fast grabbing and tossing of an object: Proposing a new approach," *IEEE Robotics Automation Magazine*, vol. 29, no. 3, pp. 127–138, 2022.

[10] V. Kumar and K. J. Waldron, "Force distribution in closed kinematic chains," *IEEE Journal on Robotics and Automation*, vol. 4, no. 6, pp. 657–664, 1988.